Title

Radiation burn-through measurements to infer opacity at conditions close to the solar radiative zone-convective zone boundary

Authors

D. J. Hoarty[1]*, J. Morton[1], J. C. Rougier[1,2], M. Rubery[1,3], Y. P. Opachich[3], D. Swatton[1], S. Richardson[1], R. F. Heeter[3], K. McLean[4], S. J. Rose[4], T. S. Perry[5], B. Remington[3]

Affiliations

[1]AWE plc; Reading, RG7 4PR, UK.

[2] School of Mathematics, University of Bristol, Bristol, BS8 1UG, UK.

[3] Lawrence Livermore National Laboratory; Livermore, CA 94550, USA.

[4] Plasma Physics Group, Blackett Laboratory, Imperial College London; London, SW7 2AZ, UK

[5] Los Alamos National Laboratory; Los Alamos, New Mexico, NM 87545, USA

*Corresponding author. Email: David.Hoarty@awe.co.uk

Abstract

Recent measurements at the Sandia National Laboratory of the x-ray transmission of iron plasma have inferred opacities much higher than predicted by theory which casts doubt on modelling of iron x-ray radiative opacity at conditions close to the solar convective zone-radiative zone boundary. An increased radiative opacity of the solar mixture, in particular iron, is a possible explanation for the disagreement in the position of the solar convection zone-radiative zone boundary as measured by helioseismology and predicted by modelling using the most recent photosphere analysis of the elemental composition. Here we present data from radiation burn-through experiments which do not support a large increase in the opacity of iron at conditions close to the base of the solar convection zone and provide a constraint on the possible values of both the mean opacity and the opacity in the x-ray range of the Sandia experiments. The data agree with opacity values from current state-of-the-art opacity modelling using the CASSANDRA opacity code.

MAIN TEXT

Introduction

An understanding of radiative x-ray opacity is fundamental to astrophysics and plasma physics in general, including efforts to achieve fusion in the laboratory. X-ray opacity of iron is especially important in astrophysics because it has a large contribution to the overall opacity in stellar interiors. As the sun is our closest and most intensively studied star it is the benchmark for modelling stars in the wider universe, and a discrepancy in solar modelling has implications throughout astrophysics. In the last two decades there has been a revision of the solar elemental composition due to the work of Asplund and coworkers *(1-4)* studying the C, N, O, Ne, Ar and other elements on the surface of the sun, though the proportion of iron was unchanged. The revised composition resolves some anomalies *(5)*, but modelling using these new values differs from very precise helioseismic measurements *(6-8)* of the radial position of the convective zone-radiative zone boundary, which is where energy transport changes from radiative diffusion to convection. Helioseismic measurements *(9, 10)* put the boundary at 0.713±0.001 Rs where Rs is the solar radius, whereas the position predicted by theory using the new solar composition is at 0.726Rs. It has been shown that this difference could be accounted for by an increase of 15% in the mean radiative opacity at the boundary. The mean opacity in this case is the Rosseland mean typically used in stellar diffusive radiative transport simulations, which is the harmonic mean over the whole photon spectrum with a weighting function that peaks at $h\nu \approx 4T$, where T is the temperature. The energy transport is most sensitive to opacity at x-ray energies around the peak of the weighting function *(11,12)*.

An increased opacity as an explanation for the discrepancy in the solar radiative-convective zone boundary has been supported by recent measurements *(13-15)* that indicate a significant difference between the measured and predicted opacity of iron at conditions close to the base of the convective zone. Iron is believed to contribute around 20% of the opacity at the convective-radiative zone boundary, where the temperature is approximately 200eV and the electron density approaches 1e+23/cc. These measurements, carried out at the Sandia National Laboratory Z pulse power facility *(16)*, showed an iron opacity between two and four times higher than predicted by theory over most of the x-ray energy range of the measurements, between 970-1770eV, which covers the spectral region of the L shell transitions, bound-free edge and near edge bound-free continuum. If extended to lower x-ray energies this increase in iron opacity is roughly half the increase in the total mean opacity needed to resolve the solar physics discrepancy.

In addition to the solar physics discrepancy, a change in iron opacity has implications for all stars whose structures pass through conditions affected by this change in opacity. Additionally, the solar abundances serve as the standard in astrophysics so the resolution of this issue will have wide repercussions. Uncertainties extend to asteroseismology *(17)*; the calculation of luminosity variation in the search for exoplanets, and cosmological distance measures based on Cepheid variable pulsation-luminosity relations. Based on the higher opacity of iron measured on the Z facility the opacity of iron has been increased by workers modelling variable stars to explain pulsation in O and B-type stars *(18, 19)*.

Though a higher iron opacity could help explain the solar physics discrepancy, more importantly it is a cause of concern to the wider community of scientists studying the radiative properties of hot, dense matter. This difference between the Sandia iron measurements and opacity theory has significant implications for plasma opacity theory in general because it is in violation of the fundamental Thomas-Reiche-Kuhn oscillator sum rule *(20)*. There are ongoing theoretical attempts to explain the discrepancy (*21-26)*. These invoke multi-photon absorption, enhanced photoionization from states unconsidered previously, or modifications to the photoionization due to scattering at high density. But these attempts have either not demonstrated a sufficiently large effect on opacity to explain the Sandia measurements or remain controversial. In addition to theoretical efforts there is an ongoing campaign of experiments which has been running for the past six years at the US National Ignition Facility laser (NIF) *(27)* at Lawrence Livermore National Laboratory to repeat these iron experiments using techniques similar to those used for the frequency resolved transmission measurements at the Z facility *(28,29)*.

This paper describes a radiation burn-through experiment coupled with detailed radiation-hydrodynamics calculations and statistical analysis. Its purpose is to examine whether the large increase in iron opacity found in the Sandia experiment could be extrapolated to those energies most important to radiation transfer at conditions near the base of the convective zone, thereby determining if a higher iron opacity could be a partial explanation for the solar physics discrepancy. In addition, the analysis estimates the value of the iron opacity in the x-ray energy range of the Sandia measurements, based on the radiation burn-through measurements. The conclusion of the study is that the data show no evidence of an iron opacity high enough to change the radiative transfer close to the radiative zone-convective zone boundary conditions, but rather that the iron opacities agree with current opacity predictions using state-of-the-art methods. The data and analysis also set an upper limit to the possible value of the opacity in the x-ray energy range of the Sandia data that is consistent with the burn-through data.

Addressing the iron opacity anomaly

The experiments and analysis described in this paper use a technique to infer opacity different from the Sandia frequency resolved transmission measurements. In this paper the transit of a radiation-driven, supersonic, diffusive wavefront through an iron rich sample is used to infer the iron opacity from frequency-integrated, time-resolved measurements. Both the time taken for a supersonic wavefront to transit the sample, and the time-history of the emergent flux *(30)* are measured and compared to modelling to infer the opacity. In general, transmission experiments have been preferred to radiation burn-through measurements because they were believed more accurate, a more direct method to infer opacity and indicated where in the opacity spectrum discrepancies arose. However, the present case study on iron is a special case where the discrepancy is unusually large, which strongly affects the radiation transfer and is at a higher temperature than where transmission experiments have been successfully demonstrated in previous work. The radiative burn-through technique, despite its limitations, does not suffer from the high background fog level and self-emission that must be overcome in high temperature transmission experiments.

The opacity model used in the study is the AWE CASSANDRA opacity model *(31)* which uses the local-thermodynamic equilibrium approximation. Comparison of CASSANDRA simulations to the published Sandia iron data shows the same discrepancy seen with other state of the art codes. A comparison between CASSANDRA and the Sandia iron data is shown in Fig 1 plotted against wavelength to replicate the comparison of codes and Sandia data published previously *(13)*. As in the comparisons of the Sandia data with other opacity codes *(13)* at the experimental conditions, shown in Fig 1, the CASSANDRA simulations underestimate the opacity by a factor of about two over most of the spectral range, and about four in the higher transmission regions between transition arrays in the wavelength range between 10-12Å.

In Fig 1 in the bottom panel, for conditions of electron temperature 165eV, electron density 7e+21/cc, the simulated values lie at or above the experiment for wavelengths below 10Å. In this x-ray range the opacity is dominated by the bound-free contribution. At longer wavelengths the bound-bound contribution dominates and there is a difference in the details of the bound-bound structure. In the next panel up, showing results for 170eV and 2e+22/cc, the simulation is now significantly below the experiment over most of the x-ray range sampled. The experimental bound-free opacity is now twice the simulated value, and in the x-ray range between the bound-bound features in the spectrum, for example just above 11Å and just below 12Å, it is four times the simulated value. These differences persist for the conditions shown in the other panels of Fig 1. However, earlier experiments at around 160eV and 7e+21/cc showed excellent agreement with opacity predictions *(32)* indicating that the higher opacity is confined to iron plasma with electron temperatures above 165eV and electron density above 1e+22/cc. A burn-through experiment to check the Sandia data would have to attain these electron temperatures and densities.

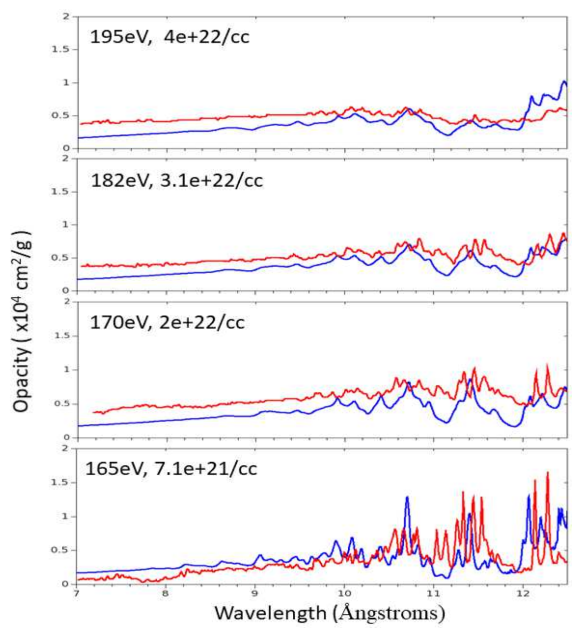

Fig 1: The iron data from the Sandia experiments from reference 13 shown in the red curves compared to simulations from the CASSANDRA opacity code (blue curves). The electron temperature and electron density taken from reference 13 are given for each of the four cases. The wavelength range is equivalent to an x-ray energy range of 970-1770eV.

The effect of an increase in the iron opacity on radiation transport depends on the opacities where the peak radiation transfer occurs, which as mentioned above is at the peak of the Rosseland weighting function. At the convective-radiative zone boundary temperature of around T= 200eV, peak diffusive radiation transport at about 4T corresponds to 16Å, which is outside the range of the Sandia data (see Fig 1). However, if the increase in the bound-free iron opacity in the range of the Sandia data extends to the bound-free opacity at lower energies, the increase in the mean opacity would affect the radiation transfer significantly. The opacity change would represent half that needed to explain the radial position of the solar radiative-convective zone boundary. The present work infers the iron opacity by performing radiation burn-through measurements at conditions close to the Sandia experiments. Though the experiments are most sensitive to x-ray opacity at energies where the radiative energy transport peaks, the study also investigates the sensitivity of the radiation burn-through to opacity changes in just the x-ray energy range of the Sandia data and sets an upper limit on the range of possible iron opacity values consistent with the data.

Fig 2 shows the total opacity spectrum for iron as simulated by CASSANDRA plotted against x-ray energy up to 2.5keV. These energies extend over the free-free opacity, the bound-free opacity above and below the L shell edge, and the bound-bound transition arrays. The CASSANDRA values are smoothed slightly due to the binning into 288 groups for input to the radiation-hydrodynamic simulations described below. In the example spectrum shown at 194eV the peak radiation transport occurs around the rising edge of the bound-bound transition array at 700-800eV. The Sandia measurements cover the range 970eV-1770eV which corresponds to the higher x-ray energies of the bound-bound transitions, the L shell bound-free absorption edge, and the bound-free continuum slope.

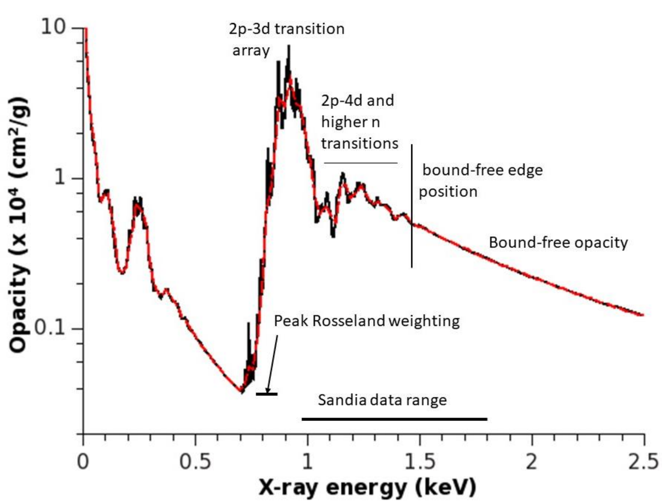

Fig 2: An example CASSANDRA simulation of the spectrum of iron before (black curve) and after (red curve) binning to a 288 group structure for the radiation-hydrodynamics simulations. The example simulation is at 194eV, 4.0e+22/cc electron density

Results/Simulation comparisons

The energy of a NIF or Z facility is required to produce a supersonic radiation-driven diffusive wave in the laboratory at the conditions of the solar convective-radiative zone boundary for sufficient time to perform the experiment *(30)*. NIF also has the diagnostics to measure both the flux driving the radiation wavefront and the timing and flux of the radiation breakout from the sample. Two NIF shots were awarded through the LLNL Discovery Science NIF access scheme with one shot in May 2020 (200525-002) and one in February 2021 (210210-001). To convert laser energy into a suitable x-ray radiation field to drive the experiment, beams of the NIF laser were directed into a gold hohlraum. Laser driven hohlraums have been in use for decades in inertial confinement fusion and related research *(33)*. The hohlraum configuration was adapted from one used previously on NIF *(34)* and uses the halfraum design where beams enter through a single laser entry hole (LEH) in a gold cylinder, with the sample package mounted on the opposite side of the cylinder. The dimensions of the cylinder are 3.5 x 3mm as shown in the Fig 3(a), with 25µm thick gold walls and a 2.4mm LEH. Fig 3(a) also shows the schematic layout of the target, laser beams, and diagnostics. The two shots each used a total of 64 beams of 0.351µm wavelength light in two cones of 32 beams at 44.5º and 50º from the cylinder axis. The shots had total delivered energies of 219kJ (shot 200525) and 286kJ (shot 210210).

The experimental foam sample was designed to have a density such that the radiation flow is supersonic and diffusive and therefore sensitive to the opacity of iron, but not so high that the radiation front propagation could become subsonic (where a shock is driven ahead of the radiation front) or transonic (where a compression moves with the radiation front), because this introduces additional uncertainty and model-dependency on the values of the density and equation of state. This precludes the use of a solid density iron foil, because even on NIF there is insufficient energy to drive a supersonic wave in a solid density iron sample, which in any case would be at the wrong density to simulate the convective zone boundary conditions. Rather than use an iron foam, which would be subject to unknown oxidation and could be potentially unstable, stable iron oxide foam was fabricated that could be accurately characterized ahead of the experiments. The iron oxide foams were manufactured at AWE and characterized using a variety of techniques to establish the foam density and composition (see Materials and Methods for more details). The intention in the foam manufacture was to produce samples of Fe_2O_3. However, characterization showed the foam had a lower iron content, 50% by weight rather than the 70% by weight expected with Fe_2O_3, with a chlorine contamination of 7% by weight, carbon of 2% by weight, and the remainder oxygen. The equation of state and opacity were modelled using this characterization of the foam (see Suppl. Materials). The chlorine contamination was found to have a negligible effect on the radiation burn-through measurements. The foam density was chosen so that once heated the electron density in the foam replicated that of the Sandia transmission experiments. To select the samples, the foam uniformity was measured with x-ray tomography (see Materials and Methods). The average foam density on the two shots was 134.4mg/cc (200525) and 164.3mg/cc (210210), each ± 2% and the x-ray tomography confirmed the high degree of uniformity in the samples selected (see Suppl. Materials)

The radiation temperature in the hohlraum was measured using the NIF DANTE *(35)* calorimeter/spectrometer, which uses an array of filtered x-ray diodes to give eighteen channels that record time-resolved x-ray fluxes emitted from the hohlraum through the LEH. The experiment measured the hohlraum temperature with the NIF DANTE 1 instrument viewing at 37º to the hohlraum axis. A 2mm diameter, 1mm long gold cylinder filled with the iron oxide foam was attached to the hohlraum so that the radiation flux from the hohlraum drove a supersonic radiation wave through the foam and along the length of the cylinder to emerge at the rear surface. The arrival time and emergent flux of this radiation at the rear of the foam were measured by the NIF DANTE2 instrument viewing at 64º to the cylinder axis. To establish the arrival time accurately a separate laser beam irradiated the outside of the gold cylinder at a known delay after the start of the laser beams used to heat the hohlraum. This produces an x-ray signal that is recorded on DANTE2 (see Fig 3(a)) and can show the timing of the radiation break-out with respect to the heating beams to an accuracy of 100ps. This is a standard technique used at NIF to provide an accurate timing reference for DANTE2. Both sets of DANTE measurements were converted from diode output voltages to x-ray fluxes measurements using the UNSPEC-chi unfold routine *(36)*. The spatial uniformity of the radiation wave break-out at the end of the tube was measured using a four-channel gated x-ray imager, which showed a high degree of uniformity across the front. Error bars of ±10% on the DANTE measurements are due to the uncertainty in the flux level based on the sensitivity calibration of the DANTE photocathodes, filters, and mirrors. The two shots had different laser pulses, to compensate for differences in the foam density on the two shots and to ensure supersonic wave propagation in the foam. These are shown in Fig 3(b) and the resulting simulated radiation drive expressed as a radiation brightness temperature is shown in Fig. 3(c).

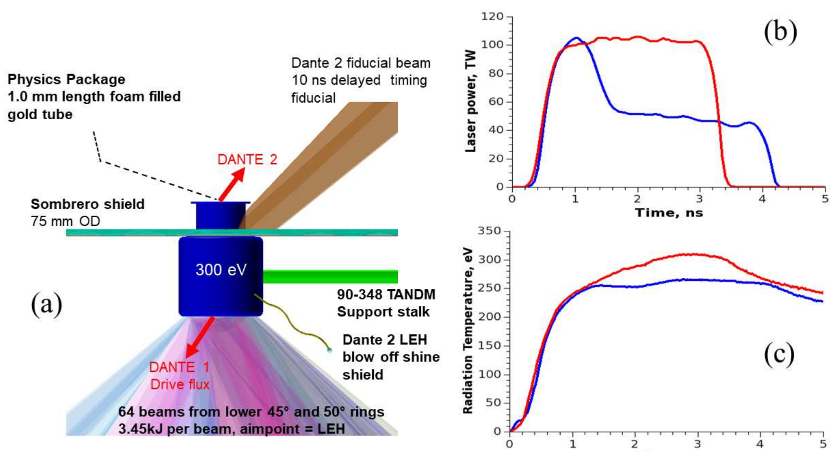

Fig 3: (a) shows a schematic of the gold hohlraum and physics package; (b) shows the measured laser pulse shapes used on the two shots (blue curve 200525; red curve 210210); (c) shows the resulting simulated hohlraum radiation brightness temperatures.

To analyse this experiment and better understand the contribution of the iron opacity, the experimental data were compared to simulations using the NYM *(37)* code. NYM is a two-dimensional Lagrangian code, with an Implicit Monte Carlo direct numerical simulation method *(38)* for the x-ray transport where energy is transported via tracking particles that represent the absorption and re-emission of the radiation photon flux. The simulations were fully integrated with laser, hohlraum, and the passage of the radiation-driven front along the foam-filled tube in the same simulation. The laser ray tracing was two dimensional and the energy deposition modelled to calculate the laser absorption in the hohlraum by inverse bremsstrahlung and resonance absorption. The code calculates x-ray emission from the laser spots by calculation of the electron thermal conduction into the hohlraum wall, using a flux-limited thermal diffusion model and non-local thermodynamic equilibrium equation of state and opacity from a screened hydrogenic average atom atomic physics model *(39)* to calculate re-emission from the wall area of the laser spots.

The absorption and re-emission of radiation from the hohlraum walls away from the laser spots is calculated using gold opacities from the opacity code CASSANDRA. Using CASSANDRA data NYM calculates the diffusive radiation wave propagation into the hohlraum walls. At the radiation temperatures achieved in this experiment the depth of the radiation penetration into the hohlraum wall exceeds a mean free path across the entire radiation spectrum, and therefore the wall re-emission is a Planckian radiation field. In addition to the Planckian field, there is a non-thermal component to the hohlraum radiation field which comes from the gold M-shell emission from the ablation surface of the laser spots. The effect of this non-thermal component was investigated and found to have a negligible effect on the wavefront propagation *(30).*

In the radiation transport through the foam, the foam opacity is dominated by the opacity of iron. The opacity of the foam is calculated by combining the opacities in the mixture on an electron density grid, with the opacities of oxygen and other low atomic number foam constituents taken as being modelled accurately. The CASSANDRA opacities for the mixture are input to the radiation-hydrodynamics calculation as an opacity spectrum binned into 288 groups, for each temperature-density grid point in a 54x50 temperature-density grid. The bounds of the grid are minimum temperature 6.4eV; maximum 100keV; minimum density 2e-04 g/cc; maximum density 3470g/cc. CASSANDRA includes models of continuum lowering, strong-coupling and electron degeneracy but these effects do not apply at the foam conditions in these experiments. The grid is linear in log space; interpolation is in log-log space. The group-widths are narrow at frequencies where the opacity changes rapidly, due to bound-bound transitions and bound-free edges. Where the opacity is near constant over a wider frequency range, for example in frequency ranges where the opacity is dominated by bound-free absorption far from edge structure, the group-widths are wider. The high number of groups ensures convergence of the radiation transport simulation and captures the spectral features of the iron, as shown in Fig 2. Sensitivity studies *(40)* show that convergence of the radiation propagation simulation requires at least 20 groups for the iron spectrum at the experimental conditions, and single group (grey) Rosseland mean opacity simulation significantly underestimates the transit time of the radiation front. As previously stated, NYM does not use the diffusion approximation but calculates radiation transport using an Implicit Monte Carlo method *(38)* using the group structure as described above. The equation of state is interpolated from tables generated using the NuQEOS model *(41)*.

The NYM two-dimensional radiation-hydrodynamics simulations assumes cylindrical symmetry, and accounts for the radiation coupling factor from the hohlraum to the end of the foam and the radiation wavefront in its subsequent propagation along the foam filled tube. The energy input to simulation is benchmarked to measurements by comparing the simulated x-ray emission pulse in the direction of DANTE1 with the measured values. The energy is treated as a free parameter to be adjusted until agreement is obtained with DANTE1. It was found that agreement was obtained between DANTE1 and the simulation with little or no adjustment to the input laser energy.

Simulations using the NYM code are shown in Fig 3(c) and Fig 4, for the two shots in the experiment. In these simulations the sample densities are set to their measured values; the laser energy is set to its adjusted value; the sample opacity is set to its theoretical value according to the CASSANDRA code, and the equations of state are set to their theoretical values according to the NuQEOS code. Below, we refer to these as the 'nominal' values of the simulation inputs.

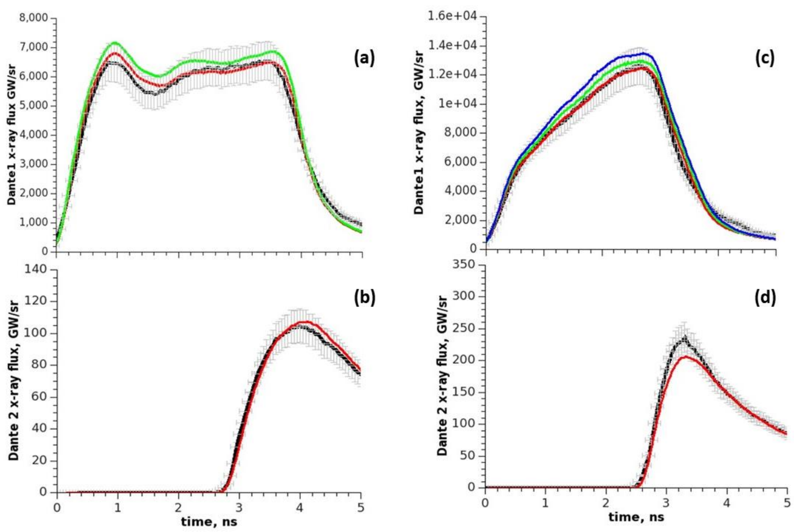

Fig 4: DANTE1 and DANTE2 results (black curves with error bars) for shot 200525, (a) and (b) respectively, and shot 210210, (c) and (d), compared to NYM radiation hydrodynamics simulations at the nominal values of opacity, density, equation of state. The simulated curve in red in 4(b) is the result of using the radiation drive that produced the red curve in 4(a), which was nominal energy scaled by 0.95. Similarly, the red curve in 4(d) is the result of using the radiation drive corresponding to the red curve in 4(c) which used the nominal unscaled energy. Also shown are the comparisons for nominal value of the energy in 200525 (green curve in 4(a)) and the effect of scaling the nominal energy on 210210 by 1.05 (green curve in 4(c)) and 1.1 (blue curve in 4(c)).

The comparison between simulation and DANTE1 data, with error bars, for shot 200525 shows good agreement for the simulation with the nominal laser energy but improves with a 5% reduction, which is within the measurement uncertainty. In the case of the second shot 210210 no such reduction was necessary for the simulation to replicate the measured hohlraum emission. This gives confidence that the simulation is replicating the hohlraum behaviour and hence the flux driving the radiation wavefront in the foam. Figs 4(b) and 4(d) show the predicted arrival time and flux profile measured by DANTE2 with error bars compared to simulation where the laser energy was scaled by 0.95 and 1 respectively to best fit the DANTE1 results. The measured burn-through profile is reproduced well in both cases by the simulation.

Fig 5 shows the simulated conditions for the iron oxide foam during the passage of the radiation wavefront using the NYM simulation at its nominal inputs. The conditions are shown for the two shots at three times during the wavefront propagation, +1ns, 2ns and 2.5ns after the start of the laser pulses into the hohlraum. The solid lines in the figure show the electron temperature profile. This shows a steep wavefront typical of diffusive radiation fronts, which are termed Marshak waves (*42, 43*). In this type of radiation wavefront, the opacity of the heated material behind the front, through which radiation diffuses, determines the wavefront behaviour. For the profiles in both shots at 1ns (solid black curves) a foot can be seen ahead of the main temperature rise in the wavefront. This is a feature from the propagation of the higher frequencies in the radiation spectrum from the hohlraum which have a longer mean free path. In the experiment this serves the useful purpose of heating the foam ahead of the main wavefront so that the pores in the iron oxide foam close before the passage of the main wavefront, negating the need to model the pore structure in the foam. The foam pore size is around 1 micron and these close in a few tens of picoseconds based on the foam sound speed. The flux in the foot ahead of the main step in the wavefront is below the detection threshold of the DANTE2 diagnostic, which is 8GW/sr, corresponding to a radiation brightness temperature around 50eV.

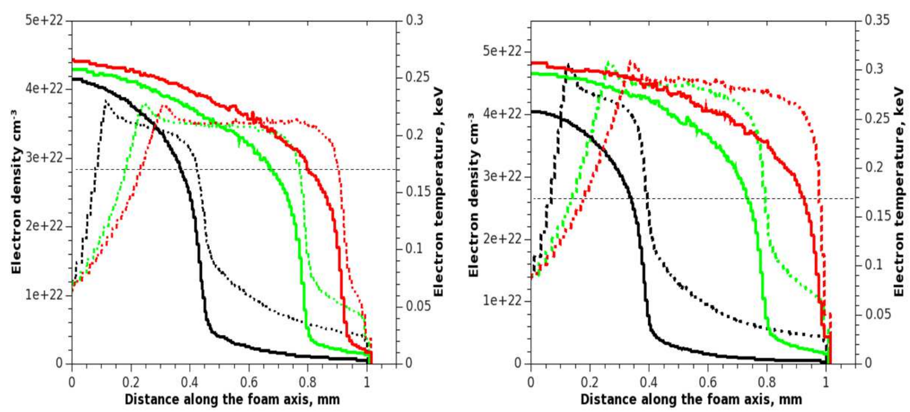

Fig 5: Simulated electron density (dotted curves, left-hand scale) and electron temperature (solid curves, right-hand scale) profiles in the iron oxide foam at three times during the radiation driven wavefront propagation along the 1mm long tube. The left pane is shot 200525 and the right pane is 210210. The three times are +1ns, black curves; +2ns, green curves and +2.5ns, red curves.

The dotted lines show the electron density behind the radiation wavefront, which is between about 1e+22 and 3.6e+22 electrons/cc in 200525 and between 1.5e+22 and 4.8e+22 electrons/cc for 210210. These electron densities are similar to the density range in the Sandia experiments, as shown in Fig 1. The temperature behind the wavefront ranges from 150eV-250eV in shot 200525 and 150-300eV in shot 210210. Hence the iron plasma opacity determining the wavefront propagation is in the range of the iron plasma in the Sandia experiments, and close to radiative-convective zone boundary conditions. The wavefront propagates supersonically through the foam followed by a rarefaction wave moving at the local sound speed in the foam plasma. Behind the rarefaction the foam density, and hence the electron density, falls. The opacity of the hotter, lower-density plasma is significantly lower than the hot, dense plasma ahead of it, and therefore it is the opacity of this hot, dense plasma which dominates the wavefront behaviour. The opacities at the different conditions as simulated by CASSANDRA are shown as Rosseland Mean values in Table S1 of Suppl. Materials.

The horizontal line on Fig 5 denotes the 170eV electron temperature threshold above which the Z facility experiments observed a significant increase in the iron opacity. Note, in the following study it is the opacity above this temperature threshold in the foam which is altered, corresponding to densities above 1e+22/cc. This is because earlier data on iron transmission in colder, lower-density plasma *(32)* from experiments also performed on the Z facility, obtained excellent agreement with theory, in the range 7-15Å, with electron temperature 156±6eV and electron density 7e+21/cc. Profiles at later times have been removed for clarity but are included in the Suppl. Materials (see Fig. S5).

The agreement between the DANTE experimental data and the NYM simulation at the nominal values of the inputs is very good. However, it does not reveal the full range of input values which are consistent with the DANTE data, taking account of the DANTE measurement accuracies, and other uncertainties. For example, it does not reveal whether values of iron opacity much larger than nominal (i.e., much larger than those based on current theory) are also consistent with the DANTE measurements. A statistical analysis combining the DANTE measurements with NYM simulations can allow for measurement accuracy, alongside other uncertainties. Using a statistical analysis, iron opacity can be constrained by the experimental data to rule out values which are highly improbable.

Statistical Analysis to infer the opacity

The variables that determine the propagation of the supersonic diffusive radiation wavefront can be identified by equating the energy transfer by radiative diffusion per unit area to the energy increase in an element of the material *(30).* The simulation for each shot is parameterized by these four variables, using adjustable inputs which are multipliers on the nominal values. Initially the two shots are modelled separately. Four inputs adjust the simulation settings for energy, density, opacity, and equation of state (eos). First, the flux from the hohlraum driving the radiation wave in the foam sample could deviate from the DANTE1 measured value, and this is captured by an input 'energy' multiplier which rescales the laser energy and hence simulated hohlraum flux within the constraints of the DANTE1 flux measurement uncertainty. Second, the actual effective density of the sample could deviate from the measured density, and this is captured by a 'density' multiplier. Third, the effective equation of state could deviate from the input equation of state, and this is captured by an 'eos' multiplier which is applied to the pressure and specific energy (internal energy/gram) tables used in the radiation-hydrodynamics simulations which are generated by the NuQEOS code. This captures uncertainty in the equation of state model at the experimental conditions and the small uncertainty in foam composition which was established to an accuracy of parts per million (see Materials and Methods section).

A fourth input is introduced to control the effective iron opacity, 'opacity'. This multiplier is used to scale the opacity of iron in that part of the grid of temperatures and electron densities where temperatures exceed 165eV. The full scaling was applied for temperatures of 170eV and above, with a log interpolation applied between 165 and 170eV. (The change from the nominal simulation of the DANTE2 trace due to a x2 opacity multiplier alone is shown in Suppl. Materials). As stated above, iron opacity experiments at lower temperatures and densities reported by the Sandia group showed excellent agreement with theory so opacities at these conditions were not altered *(32)*. In the analysis below, 'opacity' is described as a multiplier on the nominal CASSANDRA values in an electron temperature and electron density range similar to the Sandia experiments where discrepancies were observed (> 165eV, 1- 5e+22/cc). This scaling on the iron opacity is done prior to calculating the combined opacity of the foam mixture. The range of electron temperatures and densities in the foam during the passage of the radiation front can be seen from Fig 5.

Fig 6 shows the results of the DANTE 2 measurements, along with an ensemble of NYM simulations, where the simulation inputs have been varied within the prior ranges given in Table 1. The intention is to 'tune' the simulation inputs to the DANTE2 measurements from the two shots, in a fully probabilistic approach which also provides measures of uncertainty. In effect, this means down-weighting, statistically, combinations of input values for which the NYM simulation was too far from the DANTE2 measurements. However, the computational expense of each simulation (at least 8 hours wall clock time) precludes running the NYM simulator directly in the inferential calculation, and therefore the runs of the NYM simulations are used to train a Gaussian Process 'emulator', which replaces the NYM simulator in the calculation. The statistical analysis was performed using Bayesian inference to obtain the posterior distributions of all the inputs, including opacity. The likelihood function accounts for DANTE2 measurement error, limitations in the NYM simulations, and uncertainty in the emulator (see below and Suppl. Materials).

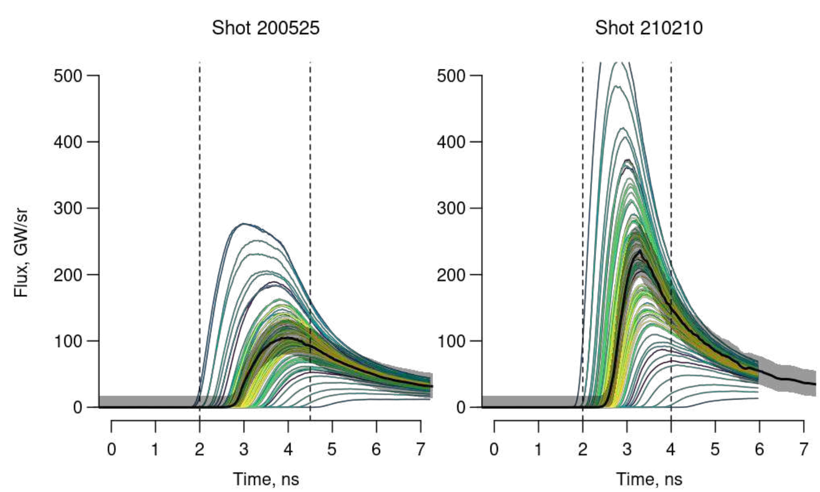

Fig 6: DANTE 2 results compared to NYM radiation hydrodynamics simulated profiles for different combinations of input values. The black curves are the measured values from DANTE2. The 'spaghetti plots' for all the simulator runs for both shots are plotted with

the experimental data. Each colour represents each batch of runs. The vertical dashed lines show the beginning and the end of the time interval used for the simulation outputs to train the emulator. The left pane is shot 200525 and the right 210210.

Figure 6 also shows the time window to select NYM simulation outputs used in the statistical analysis. The lower end of the window was defined by the time of the earliest initial rise of a simulation run. The upper end of each window is placed a little beyond the peak of the measured flux. The reliability of the simulation degrades at late time because the propagation becomes transonic as the radiation drive falls, and because of uncertainties in late time flux from the hohlraum due to stagnation of gold plasma ablated from the hohlraum walls. The output curves and measurements are thinned to one value every 0.1ns. This gives 26 time points for shot 200252 and 21 timepoints for shot 210210. The spaghetti plots of Fig 6 show the simulation outputs have a simple shape, and therefore it is not necessary to retain a large number of time-steps. Linear interpolation of the output taken at 0.1ns time-steps is indistinguishable from the full sequence of outputs.

The Bayesian inference follows the calibration approach outlined in reference *(44)*, implementing the widely used 'best input' approach *(45,46)* to find the input values that best match the DANTE2 measurements. The Bayesian inference generalizes the tuning approach based on minimizing the sum of squared residuals between the measurements and the simulation output at specified input values. The likelihood function in the Bayesian approach captures the two gaps between the measurements and the simulation output: the gap between the observations and the true values (measurement error), and the gap between the true values and the simulation output at the best input, termed the 'discrepancy'. In addition, the long run-time of the simulator requires the simulator itself to be replaced by an emulator. This introduces a third gap, between the simulation output and the emulator mean function. These three gaps are each represented by a variance matrix in the likelihood function. The measurement error variance matrix is derived from the reported DANTE2 accuracy, while the emulator variance matrix is provided by the emulator and varies with the values of the inputs. The discrepancy variance is more difficult to assess. It should be non-zero because the NYM simulation is imperfect: even at its best input, the simulation output will not perfectly replicate the true data. By incorporating the scale of the discrepancy as an extra parameter, it can be tuned to the experimental data along with the other four inputs already described. This allows the shot-to-shot variation in the discrepancy variance to be observed. The inferential calculation used a bespoke Markov chain Monte Carlo (MCMC) sampler to target the posterior distribution of the four inputs and the scale of the discrepancy.

The Gaussian Process emulators are trained on a total of 165 simulator runs (83 for 200252, 82 for 210210). One of the attractions of using an emulator is that every simulation run is useful, and while it is beneficial if the runs are space-filling in the input space, it is not crucial. Our approach for selecting the runs is described in the Statistical analysis in Suppl. Materials. Briefly, some of the runs were exploratory, and some were chosen for extra resolution in the region where the posterior probability was concentrating.

The Bayesian approach also requires a prior distribution for the inputs and the scale of the discrepancy. The input prior distributions are independent Lognormal distributions. Though opacity and equation of state are not strictly independent but are related through the plasma charge state, the NYM simulation code treats opacity and equation of state as independent variables with the tables produced by different models. The input prior distributions each have a median of 1, but with different coefficients of variation (R_v, the ratio of the standard deviation to the mean, usually labelled as C_v in statistics, but labelled here to avoid confusion with the specific heat). These R_v values are shown in Table 1. The energy and density R_v's are reported uncertainties. The EoS R_v of 1.5% allows for a small deviation away from the NuQEOS tabulation based on model-to-model variation from code comparisons *(30)*. The opacity R_v of 25% represents a large amount of prior uncertainty about the opacity multiplier: the prior 95% credible interval for the opacity multiplier is (0.613, 1.631). The prior distribution for the scale of the discrepancy, denoted 'beta' below, is exponential with a mean of 10%.

The statistical inference was applied to two case studies. In the first, designated Mallard, the opacity was scaled over all x-ray energies for electron temperatures above 170eV as described above. In the second, designated Coot, the opacity was scaled above 170eV as in the Mallard case, but only in the x-ray energy range between 970-1770eV, corresponding to the range of the data in the Sandia measurements. In each case the two shots are first considered separately and then the results are combined.

Plots of the Mallard prior and posterior probability densities for the two shots are shown in Fig 7. with summaries in Table 1. Fig 7 shows that in both shots, the main effect of the calibration is to concentrate the distribution of the opacity multiplier relative to its prior distribution. The values are concentrated around 1.0 which indicates that DANTE2 measurements support iron opacity values that are close to the nominal CASSANDRA values. There are small adjustments in the other inputs as well. In particular, the posterior distributions of beta are shifted toward zero showing the simulations are more accurate than the initial judgement of about 10%.

The two shots can be combined into one inference. The opacity and eos inputs are the same for both shots; the other inputs differ. The energy and density inputs differ on the two shots because of the difference in the drive flux and measured density between shots. The discrepancy scales differ, as can be seen in Fig 7, possibly due to the different pulse shapes and flux levels in the two cases (see Fig. 2). Once the inference has been performed separately for the two shots, the two shots can be combined simply by adding their log-likelihoods and making sure that the inputs to the joint log-likelihood are correctly allocated to the individual log-likelihoods (see Suppl. Materials for more details).

The resulting posterior marginal distributions are shown in Fig 8, with summaries in Table 1. Fig 8 shows the additional concentration in probability which comes from combining the two shots in the opacity multiplier, which is now quite tightly concentrated around 1.0, with a R_v of about 10%. The posterior 95% credible interval (95% CI) for the opacity multiplier is (0.81, 1.18). Therefore, the Mallard case study, where the full opacity spectrum is scaled, shows clearly that the value of the opacities in the x-ray energy range that has most influence on the radiation transport is well modelled by the CASSANDRA simulations, which in turn agree with other state-of-the-art opacity codes.

Though the Mallard case study confirms predicted opacity values where opacity has the most influence on radiation transport i.e., at around 4T, there is still a question over the Sandia data. This is because the 970-1770eV x-ray energy range in the Sandia experiments is higher than the peak in the Rosseland weighting function at 4T. Though the radiation burn-through experiments are less sensitive to opacity changes in this range, a further statistical study was carried out to examine the constraints put on the values of the iron opacity in the 970-1770eV range by the NIF experimental data. This statistical study, labelled Coot, was like the Mallard study except the opacity scaling was applied only in the x-ray energy range of 970-1770eV. The range of temperatures where the scaling was applied was the same as the Mallard case.

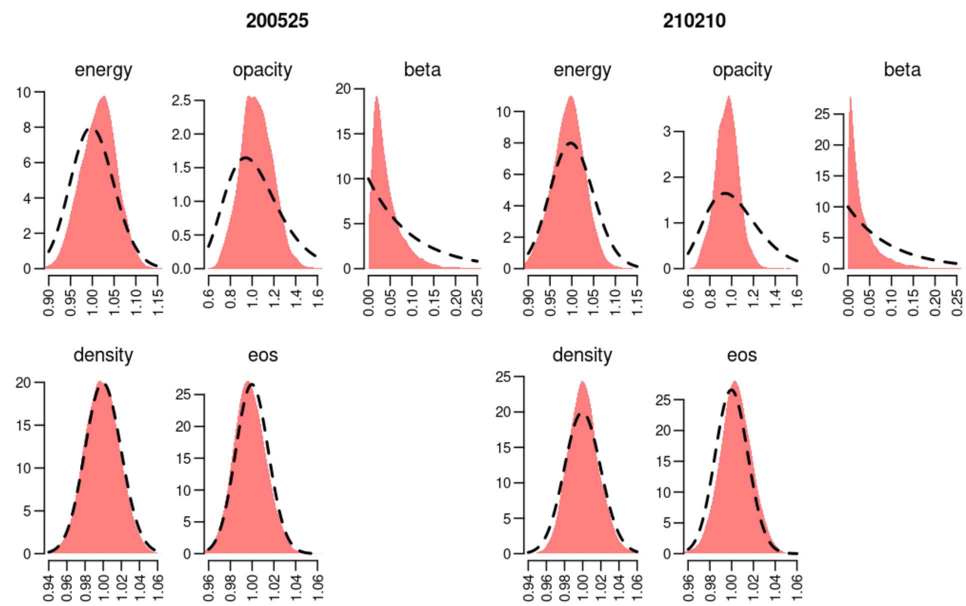

Fig 7: Probability densities for the two shots, treated separately for the Mallard case. The prior probability densities are the dashed lines, and the posterior densities are the solid shapes.

The results of the Coot statistical case study are summarized in Table 1 for the two shots separately. The prior and posterior marginal probability densities for the best inputs and discrepancy are shown graphically in the Suppl. Materials. The opacity multiplier has a larger R_v than before (a larger range) to reflect the lower sensitivity of the DANTE2 measurements to changes in opacity at the higher energy ranges

The two shots were combined in the Coot study, like in the Mallard study. Fig 9 shows the final combined results from the Coot statistical study, with summaries in Table 1. The values of the inputs are similar to the Mallard case for energy, density and eos but the lower sensitivity of the radiation burn-through data to changes in the opacity in the 970-1770eV x-ray energy range results in a larger posterior R_v. However, the posterior median value of 0.957 for the opacity multiplier is similar to the Mallard case. The posterior 95% credible interval for the opacity multiplier is (0.526, 1.797). Although the Coot study is not as constraining as the Mallard case, where the opacities scaled include those where the radiative transport is most sensitive to opacity, the experimental data does give an upper constraint on the value of the opacity under conditions similar to the Sandia transmission measurements.

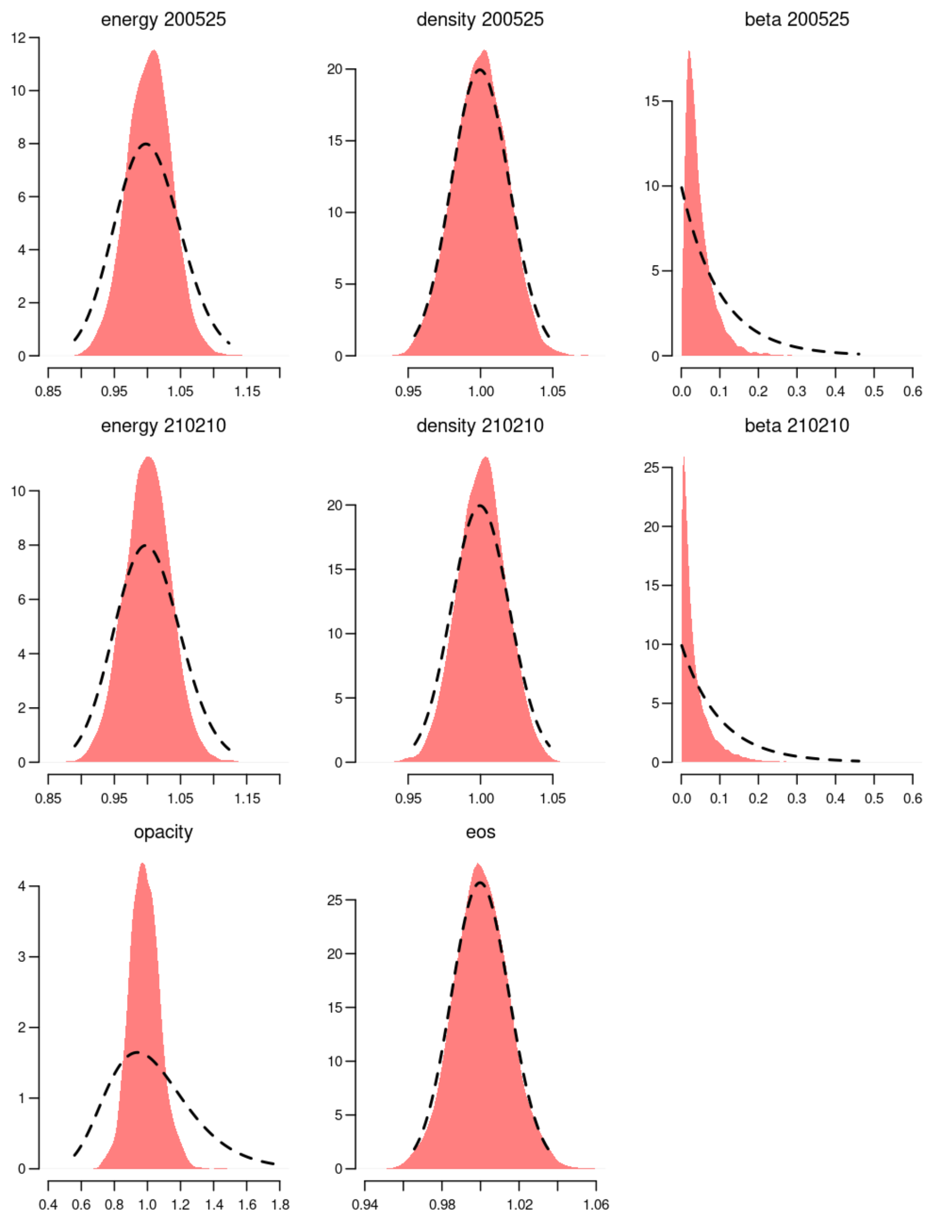

Fig 8. The marginal posterior distributions after combining the two shots in the Mallard case study. The posterior probability for the opacity multiplier is concentrated around 1; its 95% credible interval is (0.808, 1.182). The dashed lines are the prior probability densities.

MALLARD	energy	density	opacity	eos	beta	
200525 prior median	1.000	1.000	1.000	1.000	0.069	
200525 prior Rv	0.050	0.020	0.254	0.015	1.002	
200525 post median	1.014	0.996	1.040	0.997	0.032	
200525 post Rv	0.04	0.019	0.142	0.015	0.85	
210210 prior median	1.000	1.000	1.000	1.000	0.069	
210210 prior Rv	0.050	0.020	0.254	0.015	1.000	
210210 post median	0.994	1.000	0.959	1.004	0.019	
210210 post Rv	0.038	0.017	0.113	0.014	1.159	
COOT						
200525 prior median	1.000	1.000	1.000	1.000	0.069	
200525 prior Rv	0.050	0.020	0.797	0.015	1.002	
200525 post median	1.023	0.993	1.340	0.995	0.031	
200525 post Rv	0.038	0.019	0.523	0.015	0.886	
210210 prior median	1.000	1.000	1.000	1.000	0.069	
210210 prior Rv	0.050	0.020	0.795	0.015	1.000	
210210 post median	0.987	1.003	0.826	1.003	0.019	
210210 post Rv	0.038	0.016	0.358	0.013	1.182	
COMBINED SHOTS						
MALLARD	opacity	energy 200525	density 200525	energy 210210	density 210210	eos
Prior median	1.000	1.000	1.000	1.000	1.000	1.000
Prior Rv	0.250	0.050	0.020	0.050	0.020	0.0150
Post median	0.985	1.002	0.999	1.001	1.000	1.000
Post Rv	0.095	0.034	0.019	0.035	0.016	0.013
COOT						
Prior median	1.000	1.000	1.000	1.000	1.000	1.000
Prior Rv	0.700	0.050	0.020	0.050	0.020	0.0150
Post median	0.957	1.004	0.996	1.000	1.000	1.000
Post Rv	0.340	0.034	0.017	0.036	0.016	0.014

Table1: Summaries of the prior and posterior distributions of the inputs in the two case studies designated Mallard and Coot. The top half of the table shows the values for each shot separately. The bottom of the Table has the values after combing the shots in the inference. The prior distributions are Lognormal. The coefficient of variation, denoted R_v, is the ratio of the standard deviation to the mean.

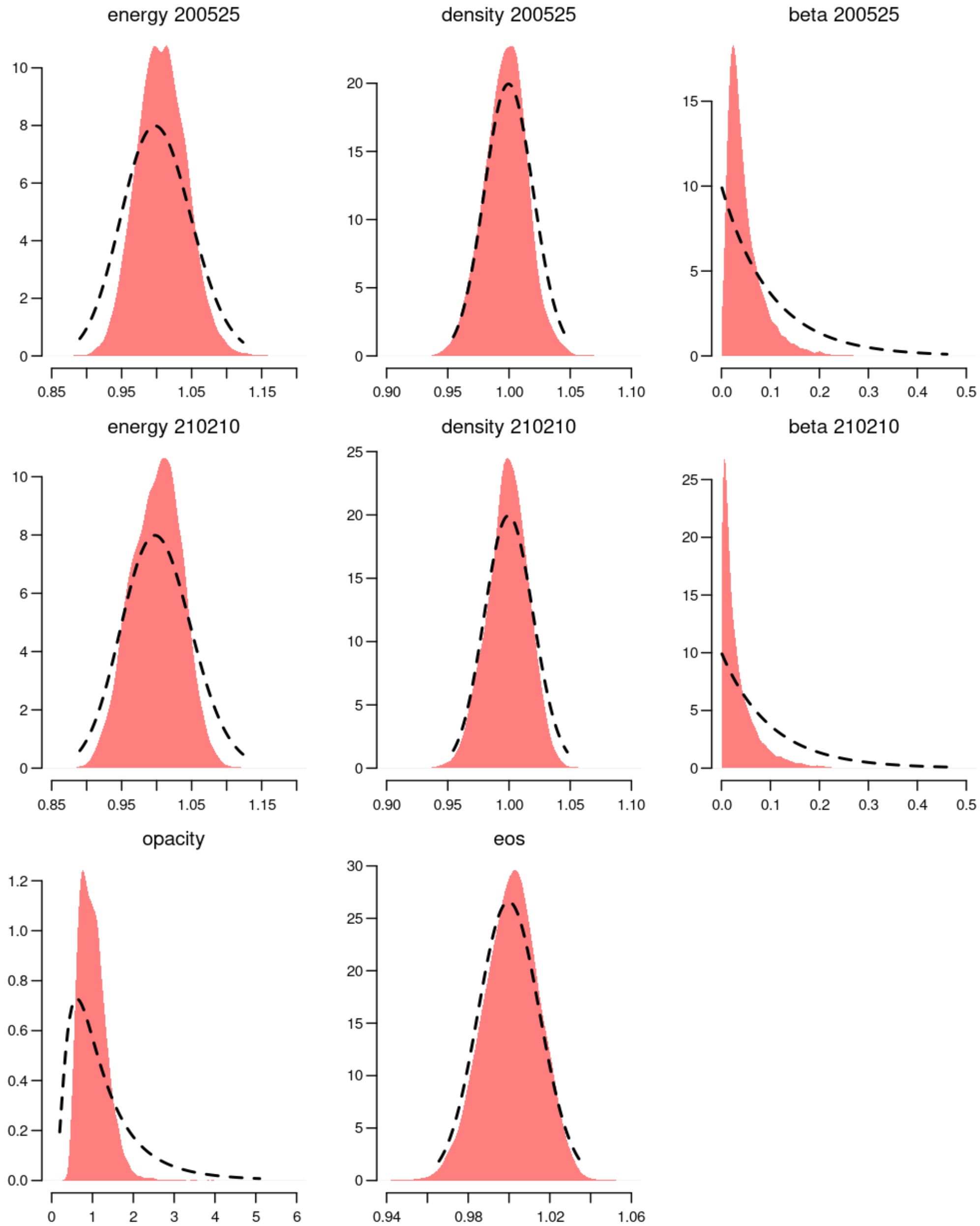

Fig 9: The marginal probability densities after combining the two shots of the Coot case study. The posterior 95% credible interval for the opacity multiplier is (0.526, 1.797). The dashed lines are the prior probability densities.

Discussion/conclusion

Experimental data from radiation burn-through of an iron-rich target using the NIF laser have been used to infer iron opacity. By controlling the energy driving the radiation front and the target density, the plasma conditions sampled in the experiment were similar to those at the base of the solar convection zone, and those in transmission experiments performed at the Z pulsed power facility at Sandia National Laboratory which had shown a large discrepancy with current theory. The Z experiments appeared to support a suggestion that an increased iron opacity could, at least partly, explain a solar modelling discrepancy in the position of the radiative zone/convective zone boundary.

To infer the opacity values consistent with NIF radiation burn-through data the time-history profiles resulting from two shots were modelled using detailed 2D radiation-hydrodynamics simulations that used opacity tables generated by the CASSANDRA opacity model. The measurements were interpreted using a Bayesian statistical analysis, along with a Gaussian Process emulator trained on the simulation runs. The analysis accounted for experimental measurement error, limitations in the simulation code, and deviation of the emulator from the simulator. This allowed the opacity multiplier to be expressed as a posterior probability density, conditional on the measurements, and summarized as a posterior 95% credible interval.

Two case studies were considered. In the first study, designated Mallard, the whole opacity spectrum was scaled for temperatures above 170eV. Previous experiments at the Sandia Z facility had established that opacities up to 160eV agreed with theory, but at higher electron temperature and electron density the measured opacities were between two and four times higher than theory prediction. The plasma conditions in the NIF radiation burn through experiments were at the higher temperatures and densities where a large opacity increase was observed in the Z experiments. In the Mallard case study, where the whole opacity spectrum was scaled, the best input opacities were found to be concentrated around a multiplier of 1 i.e., the nominal value as calculated by the CASSANDRA code, with a posterior 95% posterior credible interval of (0.81, 1.18); see Fig 8 and Table 1. This result discounts an increased iron opacity large enough to alter the radiative transport in the solar interior and explain the discrepancy in the convective zone boundary position.

Energy transport by radiative diffusion is most sensitive to opacity at 4T, which is around the peak of the Rosseland weighting function. Opacities in this range are scaled in the Mallard study. However, the transmission experiments at Sandia that measured an enhanced iron opacity did so in the range 970eV-1770eV, at temperatures up to 200eV, which is significantly above the peak of the weighting function. The Mallard study therefore leaves open the question of how sensitive the NIF radiation burn-through experiments are to changes in the iron opacity in the x-ray range 970-1770eV, where the large opacity increase was observed in the Z transmission data. To establish if the value of the iron opacity in this higher frequency range can be constrained by the burn-through experiments and analysis a second case study was carried out, designated Coot.

In the Coot study the scaling of the inputs was identical to those in Mallard except the opacity was scaled only in the 970-1770eV range corresponding to the Sandia data – see Fig 1. The range of the opacity multiplier was extended to larger values to reflect the reduced sensitivity of the DANTE2 profiles to changes in opacity in the higher x-ray energy range. The opacity multiplier was still concentrated around 1, but the posterior 95% credible interval was (0.526, 1.797), larger than in the Mallard case study. The Coot experiment shows that while a significant enhancement in the opacity is not discounted, it is constrained with the most probable value being close to 1. This indicates that a factor two or more increase in the opacity of iron relative to nominal CASSANDRA values is an overestimate. Note that CASSANDRA predictions are in good agreement with other state-of-the-art opacity codes.

In summary the data and analysis described here show that a larger than predicted increase in iron opacity cannot be invoked as a partial explanation of the convective-radiative zone boundary problem in the sun. At the conditions around those shown in Fig 5, scaling opacity over the whole spectrum in a statistical numerical modelling study shows the optimum value to match the experimental data is the nominal value as calculated by CASSANDRA, with an approximately 10% standard deviation. Treating the opacity of iron as a free parameter in modelling other astrophysical phenomena *(17, 18)* is also ruled out by these findings. The authors note recently published theoretical work using density functional theory to calculate iron at the Z conditions indicates no enhancement in the opacity of iron *[47].* Furthermore, a recent development in the debate about the solar elemental abundance is the publication of a reanalysis of solar photospheric data producing abundances that differ from Asplund and remove the discrepancy with helioseismic data *[48].*

The large increase in iron opacity in the Sandia experiments appears to violate the Thomas-Reiche-Kuhn oscillator sum rule *(20).* However as shown in the Coot study which scales the opacity in the x-ray range of the Sandia experiments between 970-1770eV the opacity in that x-ray frequency range has a median value close to the nominal value predicted by CASSANDRA and with an upper limit on the posterior 95% CI of 1.797. Although this study does not preclude an increased opacity in this x-ray energy region it does provide a constraint and demonstrates it is very unlikely that the opacity can be as high as the Sandia measurements suggest.

Acknowledgments

The authors would like to acknowledge the work of the staff of the NIF facility. We would like to thank the target fabrication staff at AWE in particular S. O'Connell and A. Hughes for their work producing the foam samples. We thank L. K. Pattison, A. Wardlow, S. Mangles, and C. Iglesias for helpful discussions. Funding was provided by AWE and UK MoD and the LLNL Discovery Science NIF access scheme.

Supplementary Material:

Includes further information on the statistical analysis including building the emulator; fabrication and characterization of the foam target and CASSANDRA opacities.

Materials and Methods

Experimental Design

The experimental technique to infer opacity from radiation burn-through requires a measurement of the radiation flux driving the burn-through from one side and a measure of the timing and flux time-history of the emergent radiation from the other. The experiment was designed to replicate the plasma conditions at the base of the solar convective zone and close to previous experiments performed at the Z machine at Sandia using an iron rich foam target heated with a NIF hohlraum. The success of the experiment depended on the foam fabrication and the ability of the radiation-hydrodynamics simulation to replicate the radiation field in the hohlraum.

Foam fabrication and characterization

The gold hohlraum targets and tubes were made by coating gold onto brass mandrels. The LEH and diagnostic holes were machined using a Precitech high precision lathe and then the brass mandrels were suspended in concentrated nitric acid to dissolve the brass; washed in demineralized water; inspected to check all the brass had dissolved and metrologised. The foam sample could not be glued in place because the glue would wick into and dissolve the foam, so the tube was made with a lip and location ring. Once the foam was inserted it was held in place by a gold ring glued onto the outside of the tube. The assembly is shown in Suppl. Materials.

The iron oxide foams were manufactured at AWE and an initial measure of the density was established from metrology of the foam dimensions and weighing the foam billet from which the sample cylinder was machined. Having selected billets of the appropriate density the cylinder was machined using a Precitech precision lathe. The sample cylinder was then measured and weighed to obtain the final sample density. The balance used for the gravimetry was a Sartorius MSA2-7S ultra-microbalance and the sample diameter and length measurements used a Keyence IDMS (model IM-6225). Further testing of the sample foams for uniformity was done by x-ray tomography using a commercial Bruker x-ray source with a spatial resolution of 4µm and a commercial XRADIA source with a spatial resolution of 1µm. The foam was radiographed under rotation to allow side-on imaging and imaging of slices through the cylinder from end-to-end, with the foam held in place magnetically. Samples with any voids, cracks or high-density non-uniformities were rejected. A high degree of uniformity was achieved in the samples selected though the rejection rate of samples due to cracking under machining was high. An example of the x-ray tomography on a passed sample is shown in Suppl. Materials. Note non-uniformities at the end and edges of the sample foam radius are covered by the mounting rings in the DANTE2 view. The typical pore size in the foam is between 1-2µm which is below the resolution limit of the Bruker x-ray microscope.

Samples of the foam from the billet machining were used to establish the foam elemental composition. SEM-EDX energy dispersive x-ray fluorescence of the foam samples was carried out at both the AWE target fabrication department and Leeds University to establish elemental composition and cross-check results. This was also checked by x-ray radiography in the frequency region of the iron K-shell absorption edge carried out at AWE. The most sensitive test used inductively coupled plasma, optical emission spectroscopy, ICP-OES, and was carried out by Exeter analytical UK, University of Warwick, to measure the elemental composition to an accuracy of parts per million. All the techniques showed that the foams were not consistent with a formulation of Fe_2O_3 but had iron at only 50% by weight with a 7% contamination of chlorine and 2% by weight of carbon, the rest of the foam was comprised of oxygen. The subsequent equation of state and opacity of the foam was based on this foam composition. The slight chlorine contamination was found to be due to residual chlorine from $FeCl_3$ used in the foam fabrication process *(49)*.

CASSANDRA opacities

The values of opacity used in the NYM simulations were generated by the opacity code CASSANDRA. The iron spectrum generated in the code with a spectral resolution of 1eV was remapped onto a group structure of 288 groups over a range from 0-100keV that was used in the NYM radiation-hydrodynamics calculations. Figure 2 shows a comparison of an iron spectrum before and after the group structure binning is applied at 194eV and 4.0e+22 electron density. There is a slight smoothing of spectral features in grouping the iron spectrum otherwise the bound-bound and bound-free iron absorption features are well-resolved. The main features of the iron spectrum are the bound-bound transitions L shell transitions from 0.7-1.5keV and the underlying bound-free absorption edge. The CASSANDRA code shows a similar deviation from the Sandia data *(13)* as the other state-of-the-art codes (see Fig 1)

The CASSANDRA methodology tends to broaden bound-bound features more than a detailed line accounting treatment though oscillator strength is conserved. There is also a slight blue shift in the bound-bound spectral features in the CASSANDRA simulation compared to experiment. The values scaled in the simulations are the part of the grid at temperatures 165eV and above with a log interpolation between 165eV and 170eV. Sandia experiments showed excellent agreement with theory in experiments up to temperatures just under 160eV and so were not scaled. The bulk of the foam behind the radiation front was between 165-250eV, for the first shot, 200525 and slightly hotter 165-300eV for the second, 210210. The foam electron density range in the bulk of the foam behind the front was around 1e+22/cc - 5e+22/cc. In Suppl. Materials a table of opacities, Table S1, is shown to indicate the CASSANDRA frequency resolved opacity values used in the simulations. Values outside the conditions achieved in the experiment are shown for information.

References

1. M. Asplund, New Light on Stellar Abundance Analyses: Departures from LTE and Homogeneity, Annu. Rev. Astron. Astrophys. **43**, 481 (2005)
2. C. Allende Prieto, D. L. Lambert and M. Asplund, The Forbidden Abundance of Oxygen in the Sun, Astrophys. J. **556**, L63-L66 (2001)
3. M. Asplund, N. Grevesse, A. Jacques Sauval and P. Scott, The Chemical Composition of the Sun, Annu. Rev. Astron. Astrophys. **47**, 481, (2009)
4. P. Scott, N. Grevesse, M. Asplund, A. Jacques Sauval, K. Lind, Y. Takeda, R. Collet, R. Trampedach and W. Hayek, The elemental composition of the Sun, Astron. Astrophys. **573**, A26 (2015)
5. S. Turck-Chièze, S. Couvidat, L. Piau, J. Ferguson, P. Lambert, J. Ballot, R. A. Garcia, P. Nghiem, Surprising Sun: A New Step Towards a Complete Picture, Phys. Rev. Lett. **93**, 211102-1-211102-4, (2004)
6. S. Basu and H. M. Antia, Helioseismology and solar abundances, Phys. Rep. **45**, 217-283 (2008)

7. J. N. Bahcall, A. M. Serenelli and M Pinsonneault, How Accurately Can We Calculate the Depth of the Solar Convective Zone, Astrophys. J. 614, 464-471 (2004)
8. H. M. Antia and S. Basu, The Discrepancy between Solar Abundances and Helioseismology, Astrophys. J. **620**, L129-L132 (2005)
9. J. Christensen-Dalsgaard, D. O. Gough, M. J. Thompson, The Depth of the Solar Convection Zone, Astrophys. J. **387**, 413-437 (1991)
10. S. Basu and H. M. Antia, Seismic measurement of the depth of the solar convective zone, Mon. Not. R. Astron. Soc. **287**, 189-198 (1997)
11. D. Mihalas, Stellar Atmospheres, W. H. Freeman and Co. (1978)
12. Ya. B. Zel'dovich and Yu. P. Raizer, Physics of Shock Waves and High Temperature Hydrodynamic Phenomena, Dover (2002)
13. J. E. Bailey, T. Nagayama, G. P. Loisel, G. A. Rochau, C. Blancard, J. Colgan, Ph. Cosse, G. Faussurier, C. J. Fontes, F. Gilleron et al, A higher-than-predicted measurement of iron opacity at solar interior temperatures, Nature, **517**, 56-59 (2015)
14. J. E. Bailey, G. A. Rochau, R. C. Mancini, C. A. Iglesias, J.J. MacFarlane, I. E. Golovkin, C. Blancard, Ph. Cosse and G. Faussurier, Experimental investigation of opacity models for stellar interior, inertial fusion and high energy density plasmas, Phys. Plasmas **16**, 058101 1-15, (2009)
15. T. Nagayama, J. E. Bailey, G. P. Loisel, G. S. Dunham, G. A. Rochau, C. Blancard, J. Colgan, Ph. Cosse, G. Faussurier, C. J. Fontes et al, Systematic Study of L shell Opacity at Stellar Interior conditions, Phys. Rev. Letts. **122,** 235001 (2019)
16. M. K. Matzen, M. A. Sweeny, R. G. Adams, J. R. Asay, J. E. Bailey, G. R. Bennett, D. E. Bliss, D. D. Bloomquist, T. A. Brunner, R. B. Campbell et al, Pulsed-power-driven high energy density physics and inertial confinement fusion, Phys. Plasmas 12, 055503 1-16 (2005)
17. E. Moraveji, The Impact of Enhanced Iron Opacity on Massive Star Pulsations: Updated Instability strips, MNRAS 000, arXiv:1509.08652v1 (2015)
18. P. Walczak, Inference for stellar opacities from seismic studies of the hybrid β Cep/SPB pulsators, arXiv:1704.06067v1 1-5 (2017)
19. M. P. Di Mauro, A review on Asteroseismology, arXiv:1703.07604v2 1-31 (2017)
20. C. A. Iglesias, Enigmatic photon absorption in plasma near solar interior conditions, High Energy Density Phys. **15**, 4-7 (2015)
21. S. N. Nahir and A. K. Pradhan, Large Enhancement in High-Energy Photoionization of Fe XVII and Missing Continuum Plasma Opacity, Phys. Rev. Letts. **116**, 235003 1-5 (2016)
22. C. Blancard, J. Colgan, Ph. Cosse, G. Faussurier, C. J. Fontes, F. Gilleron, I. Golovkin, S. B. Hansen, C. A. Iglesias, D. P. Kilcrease et al, Comment on Large Enhancement in High-Energy Photoionization of Fe XVII and Missing Continuum Plasma Opacity, Phys. Rev. Letts. **117,** 249501 (2016)
23. M. K. G Kruse, C. A. Iglesias, Two-photon absorption framework for plasma transmission experiments, High Energy Density Phys. **31**, 38-46 (2019)
24. R. M. More, S. B. Hansen, T. Nagayama, Opacity from two-photon processes, High Energy Density Phys. **24**, 44-49 (2017)
25. J. C. Pain, A note on the contribution of multi-photon processes to radiative opacity, High Energy Density Phys. **26,** 23-25 (2018)
26. J. L. Zeng, C. Gao, P. Liu, Y. Li, C. Meng, Y. Hou, D. Kang and J. Yuan, Electron localization enhanced photon absorption for the missing opacity in solar interior, Sci. China-Phys. Mech. Astron. **65**, 233011 1-13 (2022)
27. C. A. Haynam, P. J. Wegner, J. M. Auerbach, M. W. Bowers, S. N. Dixit, G. V. Erbert, G. M. Heestand, M. A. Henesian, M. R. Hermann, K. S. Jancaitis et al, National Ignition Facility laser performance status, Appl. Opt. **46**, 3276 (2007)

28. T. S. Perry, R. F. Heeter, Y. P. Opachich, P. W. Ross, J. L. Kline, K. A. Flippo, M. E. Sherrill, E. S. Dodd, B. G. DeVolder, T. Cardenas et al, Replicating the Z iron opacity experiments on the NIF, High Energy Density Phys. 23, 223-227 (2017)
29. R. Heeter, T. Perry, H. Johns, Y.P. Opachich, M. Ahmed, J. Emig, J. Holder, C. A. Iglesias, D. Liedahl, R. London et al, Iron X-ray Transmission at Temperature Near 150eV Using the National Ignition Facility: First Measurements and Paths to Uncertainty Reduction, Atoms **6**, 57-77 (2018)
30. D. J. Hoarty, J. Morton, M. Jeffery, L. K. Pattison, A. Wardlow, S. P. D. Mangles, S. J. Rose, C. A. Iglesias, Y.P. Opachich, R. F. Heeter and T. S. Perry, A proposal to measure iron opacity at conditions close to the solar convective zone-radiative zone boundary, High Energy Density Phys. **32**, 70-76 (2019)
31. B. J. B. Crowley and J. W. Harris, Modelling of plasmas in an average-atom local density approximation: the CASSANDRA code, J. Quant. Spectrosc. Radiat. Trans., **71**, 257-272 (2001)
32. J. E. Bailey, G.A. Rochau, C. A. Iglesias, J. Abdallah Jr, J. J. MacFarlane, I. Golovkin, P. Wang, R, C, Mancini, P. W. Lake, T. C. Moore et al, Iron Plasma Transmission Measurements Above 150eV, Phys. Rev. Letts. 99, 265002 (2007)
33. J. D. Lindl, P. Amendt, R. L. Berger, S. G. Glendinning, S. H. Glenzer, S. W. Hann, R. L. Kauffman, O. L. Landen and L. J. Suter, The physics basis for ignition using indirect-drive targets on the National Ignition Facility, Phys. Plasmas **11**, 339 (2004)
34. A. S. Moore, T. M. Guymer, J. Morton, B. Williams, J. L. Kline, N. Bazin, C. Bentley, S. Allan, K. Brent, A. J. Comley et al, Characterization of supersonic radiation diffusion waves, J. Quant. Spectrosc. Radiat. Trans., **159**, 19-28 (2015)
35. E. L. Dewald, K. M. Campbell, R. E. Turner, J. P. Holder, O. L. Landen, S. H. Glenzer, R. L. Kauffman, L. J. Suter, M. Landon, M, Rhodes and D. Lee, Dante soft-x-ray power diagnostic for National Ignition Facility, Rev. Sci. Instrum. **75**, 3759-3761 (2004)
36. Y. P. Opachich, E. S. Dodd, R. F. Heeter, C. D. Harris, H. M. Johns, J. L. Kline, N. S. Krasheninnikova, M. J. May, A. S. Moore, M. S. Rubery et al, DANTE as a primary temperature diagnostic for the NIF iron opacity campaign, Rev. Sci. Instrum. **92**, 033519 (2021)
37. P. D. Roberts, S. J. Rose, P. C. Thompson and R. J. Wright, The stability of multiple-shell ICF targets, J. Phys. D, **13**, 1957-69 (1980)
38. J. A. Fleck and J. D. Cummings, An implicit Monte Carlo scheme for calculating time and frequency dependent nonlinear radiation transport, J. Comput. Phys. 8, 313-342 (1971
39. W. A. Lokke and W. H. Grasberger, XSN-Q: a non-LTE emission and absorption coefficient routine, UCRL-52276 (1977), https//doi.org/10.2172/7299968
40. K McClean PhD thesis, https://spiral.imperial.ac.uk/handle/10044/1/92210
41. S. D. Rothman, K. Parker, C. Robinson and M. D. Knudson, Measurement of a release adiabat from~8Mb in lead using a magnetically driven flyer impact, Phys. Plasmas, **11**, 5620 (2004)
42. R. E. Marshak, Effect of radiation on shock wave behaviour, Phys. Fluids **1** (1958)
43. A. P. Cohen, G. Malamud and S. I. Heizler, Key to understanding supersonic radiative Marshal waves using simple models and advanced simulations, Phys. Rev. Research **2**, 023007 (2020)
44. M. C. Kennedy and A. O'Hagan, Bayesian calibration of computer models, Journal of the Royal Statistical Society, Series B, **63**, 425-450. With discussion 450-464, (2001)
45. M. Goldstein and J. C. Rougier, Probabilistic formulations for transferring inferences from mathematical models to physical systems. SIAM Journal on Scientific Computing, **26**(2) 467-487 (2004)

46. M. Goldstein and J. C. Rougier, Reified Bayesian modelling and inference for physical systems. Journal of Statistical Planning and Inference, **139**, 1221-1239. With discussion 1243-1256 (2009)
47. V. V. Karasiev, S. X. Hu, N. R. Shaffer and G. Miloshevsky, First-principles study of L-shell iron and chromium opacity at stellar interior temperatures, Phys. Rev. E **106**, 065202 (2022)
48. E. Magg, M. Bergemann, A. Serenelli, M. Bautista, B. Plez, U. Heiter, J. M. Gerber, H. G. Ludwig, S. Basu, J. W. Ferguson et al, Observational constraints on the origin of the elements, Astronony & Astrophysics, **661,** A140 (2022)
49. A. V. Arrufat, M. Budziszewska, C. Lopez, A.Nguyen, J. Sitek, P. Jones, C. Shaw, I. Hayes, G. Cairns and G. Leighton, REACH compliant epoxides used in the synthesis of Fe(III)-based aerogel monoliths for target fabrication, High Power Laser Science and Engineering, **5** e24 1-6 (2017).
50. J. C. Rougier, Probabilistic inference for future climate using an ensemble of climate model evaluations, Climatic Change, **81**, 247-264
51. T. J. Santner, B. J. Williams and W. L. Notz, The Design and Analysis of Computer Experiments, Springer, New York, NY, USA, 2nd edition (2018)
52. G. Casella and R. L. Berger, Statistical Inference. Pacific Grove, CA: Duxbury, 2nd Edition (2002)
53. S. N. Wood, Generalized Linear Models: An Introduction with R. CRC Press, Boca Raton FL, USA, 2nd edition (2018)
54. B. Sansó, C. Forest and D. Zantedeschi, Inferring climate system properties using a computer model, Bayesian Analysis, **3**(1), 1-38 with discussion, pp 39-62 (2008)
55. J. C. Rougier, Discussion of "Inferring climate system properties using a computer model by Sansó et al 2008" Bayesian Analysis 3 (1), 45-56 (2008)
56. G. Golub and C. Van Loan, *Matrix Computations,* John Hopkins University Press, Baltimore MD, USA, (1996) 3rd revised edition.
57. D. Higdon, J. Gattiker, B. Williams and Maria Rightley, Computer model calibration using high-dimensional output, Journal of the American Statistical Association, **103**, 570-583 (2008)
58. J. C. Rougier, Efficient Emulators for Multivariate Deterministic Functions, Journal of Computational and Graphical Statistics, **17**(4), 827-843 (2008)
59. J. C. Rougier, S. Guillas, A. Maute and A. D. Richmond, Expert Knowledge and Multivariate Emulation: The Thermosphere-Ionosphere Electrodynamics General Circulation Model (TIE-GCM), Technometrics **51**(4), 414-424 (2009)
60. R. M. Neal, Regression and Classification using Gaussian process priors. In Bayesian Statistics 6, 475-501, editors J. M. Bernardo, J. O. Berger, A. P. Dawid and A. F. M. Smith, Oxford University Press (1999)
61. R. M. Neal, Slice Sampling, The Annals of Statistics, 31 (3) 705-741 (2003)
62. M. Gu, X. Wang and J. O. Berger, Robust Gaussian stochastic process emulation, Annals of Statistics, **46**(6A), 3038-3066 (2018).
63. M. Gu, J. Palomo and J. O. Berger, RobustGaSP: Gaussian stochastic process emulation in R, The R Journal **11** (2019).
64. R Core Team, R: A language and environment for statistical computing. R Foundation for Statistical Computing, Vienna, Austria https://www.R-project.org/ (2020)

Funding: Funding was through the authors' respective laboratories.

Author contributions:

Conceptualization: DJH, JM

Methodology: DJH, JM, JCR, MR, DS, SR, K McL
Investigation: DJH, JM, MR, KO
Formal analysis: JM, JCR, MR, DJH
Resources: DJH, RFH, TSP, BR
Visualization: JCR, DJH, JM
Funding acquisition: DJH, BR
Project administration: DJH, BR
Supervision: DJH, RFH, TSP
Writing – original draft: DJH, JCR
Writing – review & editing: DJH, JCR, SJR

Competing interests: Authors declare that they have no competing interests.

Data and materials availability: All data and code are available in the main text or the Suppl. Materials.

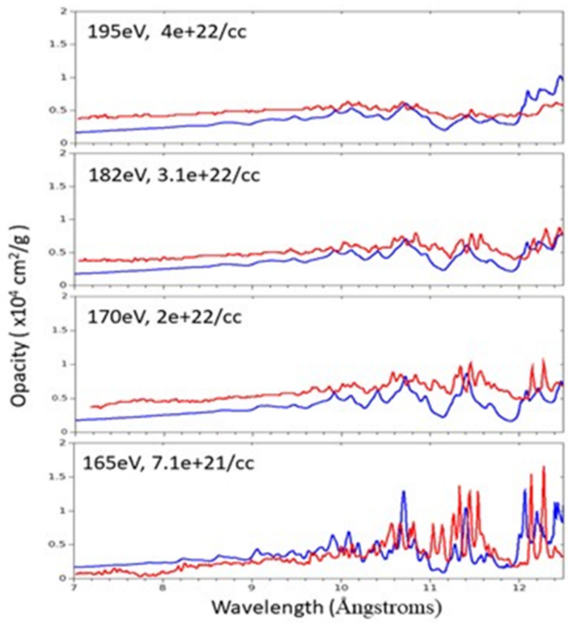
195eV, 4e+22/cc
182eV, 3.1e+22/cc
170eV, 2e+22/cc
165eV, 7.1e+21/cc
Opacity (x10⁴ cm²/g)
Wavelength (Ångstroms)

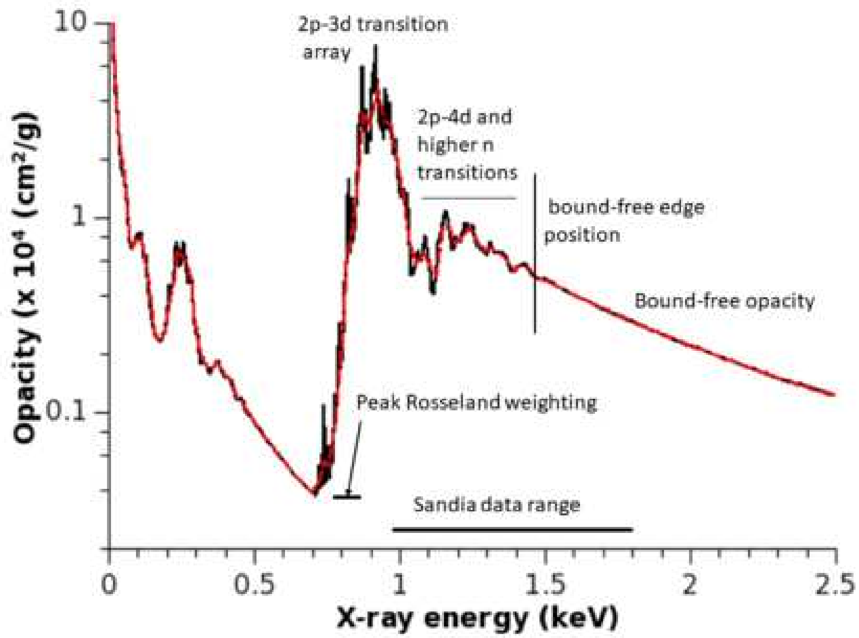
2p-3d transition array
2p-4d and higher n transitions
bound-free edge position
Bound-free opacity
Peak Rosseland weighting
Sandia data range
Opacity (x 10⁴ (cm²/g))
10
1
0.1
0
0.5
1
1.5
2
2.5
X-ray energy (keV)

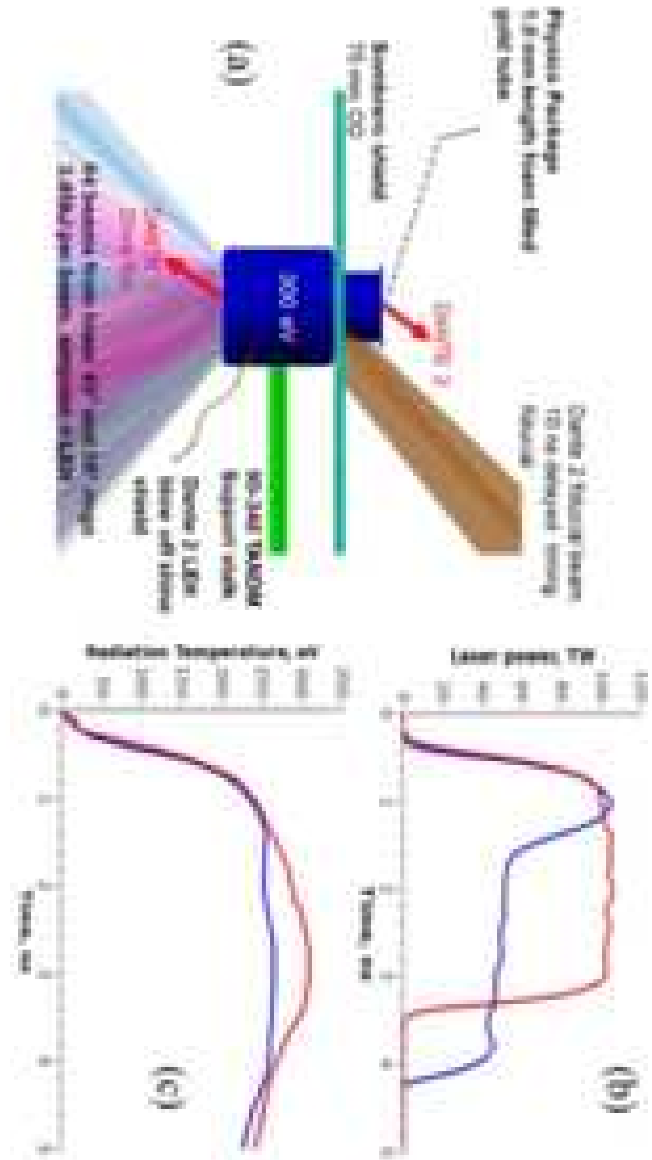
(a)
(b)
(c)
300 eV
Time, ns
Laser power, TW
Radiation Temperature, eV

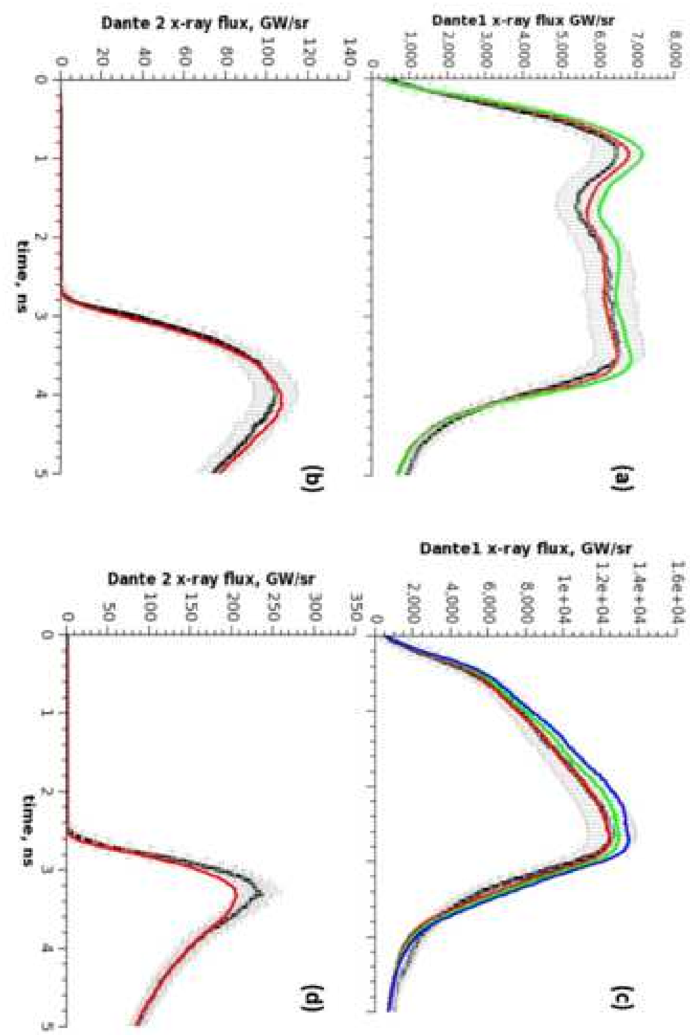
(a)
(b)
(c)
(d)
Dante1 x-ray flux GW/sr
Dante 2 x-ray flux, GW/sr
Dante1 x-ray flux, GW/sr
Dante 2 x-ray flux, GW/sr
time, ns
time, ns

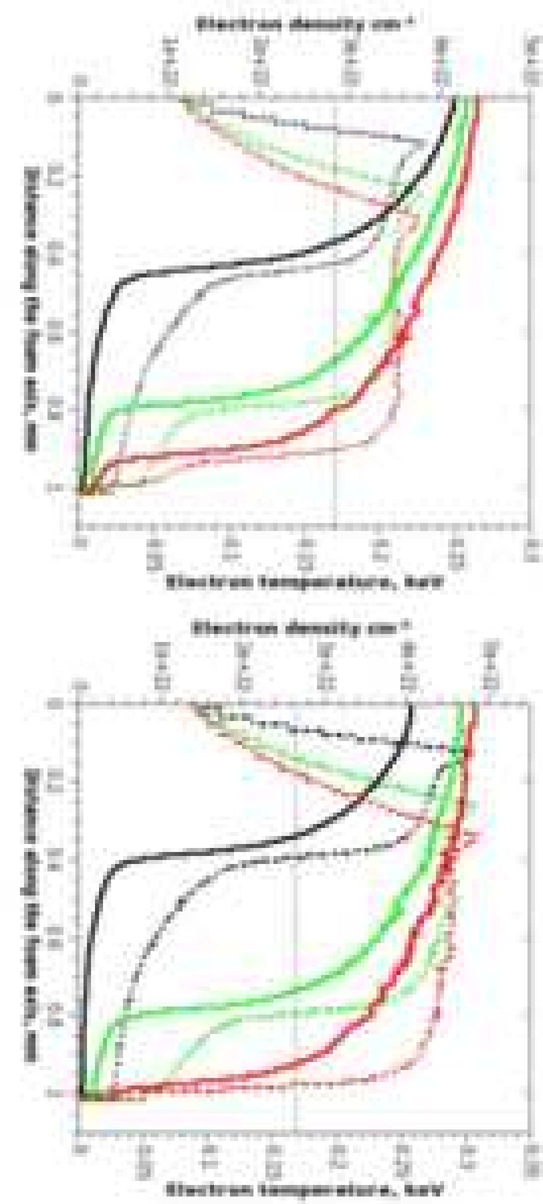
Distance along the foam axis, mm
Distance along the foam axis, mm

PLEASE CITE THIS ARTICLE AS DOI: 10.1063/5.0141850

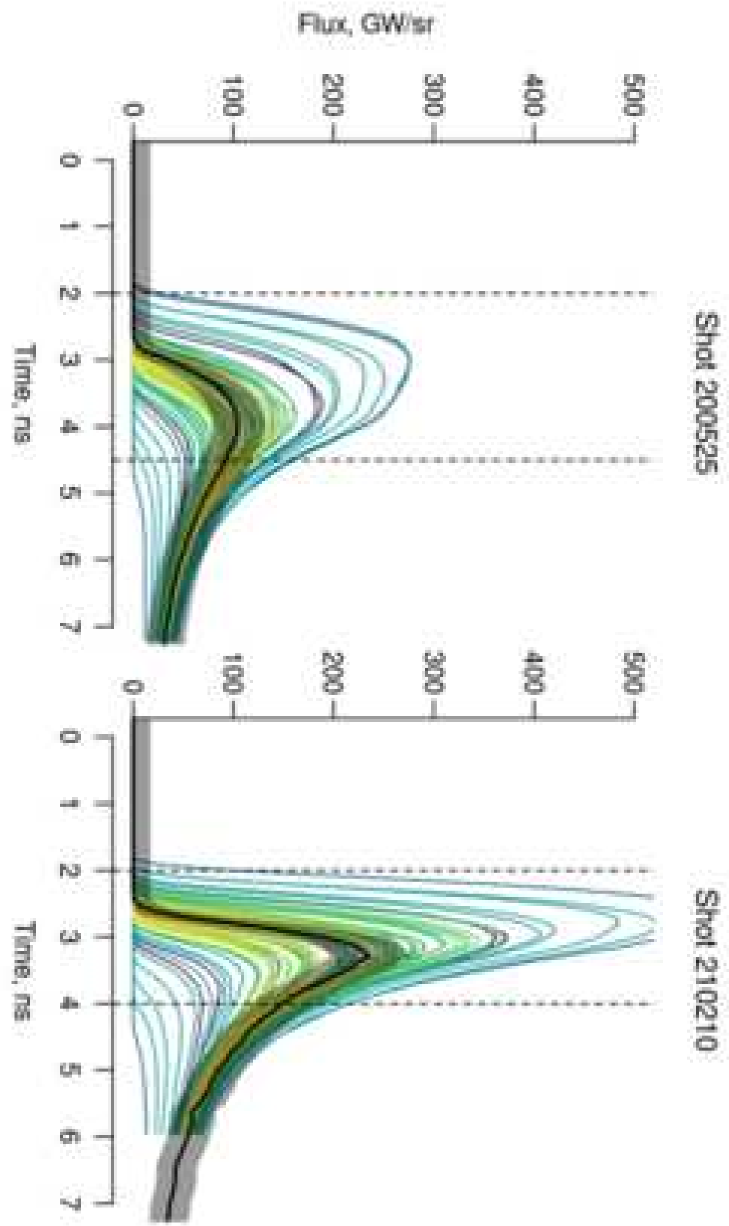

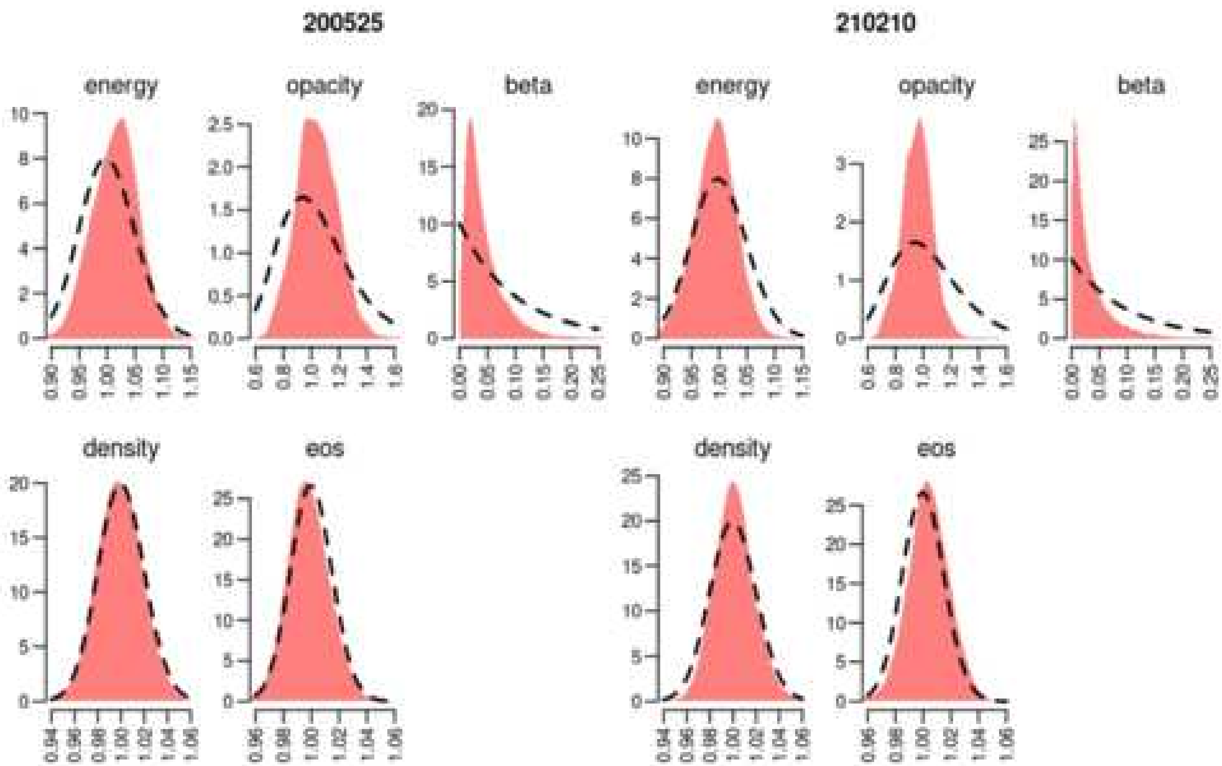
200525
210210
energy
opacity
beta
energy
opacity
beta
density
eos
density
eos

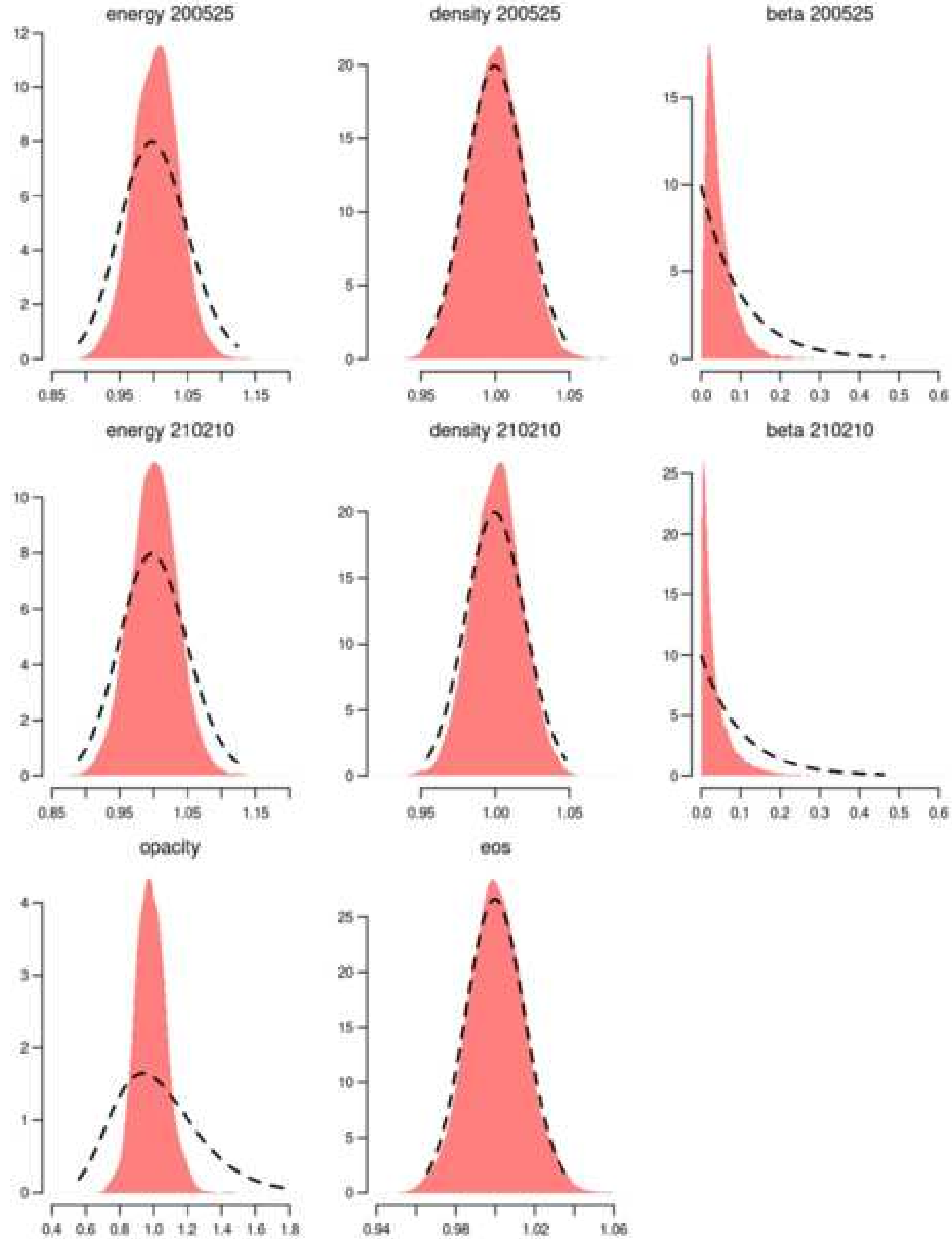
energy 200525
density 200525
beta 200525
energy 210210
density 210210
beta 210210
opacity
eos

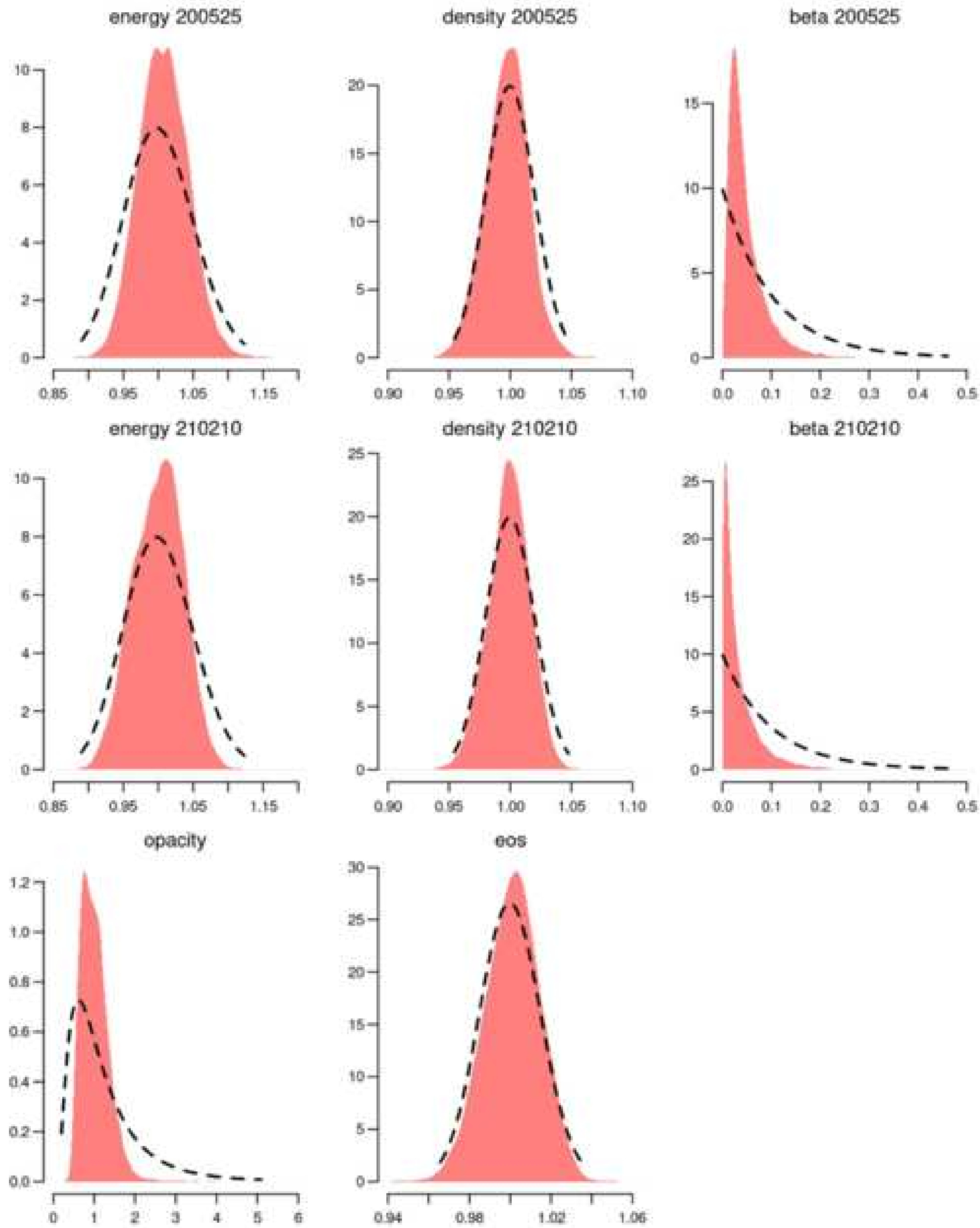
energy 200525
0.85 0.95 1.05 1.15
density 200525
0.90 0.95 1.00 1.05 1.10
beta 200525
0.0 0.1 0.2 0.3 0.4 0.5
energy 210210
0.85 0.95 1.05 1.15
density 210210
0.90 0.95 1.00 1.05 1.10
beta 210210
0.0 0.1 0.2 0.3 0.4 0.5
opacity
0 1 2 3 4 5 6
eos
0.94 0.98 1.02 1.06